pH-Responsive Near Infrared Light Triggered Hydroxyapatite Nanoparticles for Targeted Photothermal Cancer Therapy

Loganathan Palanikumar,[†,#] Faten Mansoor Yasin,[†,#] Itgel Munkhjargal,[†] Maylis Boitet,[‡] Liaqat Ali,[‡] Muhammed Shiraz Ali,[‡] Rainer Straubinger,[‡] Francisco N. Barrera,[§] Mazin Magzoub[†,*]

[†]Biology Program, Division of Science, New York University Abu Dhabi, Abu Dhabi, United Arab Emirates

[‡]Core Technology Platforms, New York University Abu Dhabi, Abu Dhabi, United Arab Emirates

[§]Department of Biochemistry & Cellular and Molecular Biology, University of Tennessee Knoxville, Knoxville, Tennessee, United States

[#] Equal Contribution

*Corresponding Author

Mazin Magzoub – Biology Program, Division of Science, New York University Abu Dhabi, Abu Dhabi, United Arab Emirates. Email: mazin.magzoub@nyu.edu, mm6432@nyu.edu

ABSTRACT

Photothermal therapy (PTT) has emerged as an effective cancer treatment strategy, which utilizes photothermal agents that accumulate at tumor sites and induce localized hyperthermia when irradiated. Near-infrared II (NIR II) fluorophores, such as the polymethine cyanine-based photothermal dye IR1061, exhibit higher temporal resolution and better tissue penetration, thereby making them promising candidates for PTT. However, challenges such as the low water solubility and *in vivo* short circulation times of these dyes limit their biological applications. To address these issues, we have developed a biocompatible and biodegradable delivery system in which IR1061 is encapsulated within lipid-coated hydroxyapatite nanoparticles (LHAPNIRs). The lipid shell is composed of DPPC/cholesterol/DSPE-PEG to retain the encapsulated dye and prevent serum protein adsorption and macrophage recognition, which would otherwise that hinder tumor targeting. Finally, the coat is functionalized with an acidity-triggered rational membrane (ATRAM) peptide for efficient and specific internalization into tumor cells in the mildly acidic microenvironment characteristic of tumors. The nanoparticles facilitated real-time thermal imaging and showed potent NIR-light triggered anticancer activity *in vitro* and *in vivo*, with no noticeable toxicity to healthy tissue. Our results demonstrate that ATRAM-LHAPNIRs (ALHAPNIRs) combine potent PTT and robust diagnostic imaging capabilities.

KEYWORDS: Cancer; diagnostic imaging; hydroxyapatite; IR-1061 dye; nanoparticles; near-infrared light; photothermal therapy; targeted drug delivery

INTRODUCTION

Traditional cancer treatments such as chemotherapy, radiotherapy, and surgical interventions have been foundational in oncology for managing solid tumors.[1–3] However, these conventional methods are often fraught with challenges, including substantial variability in patient outcomes, drug resistance, and adverse side effects.[4–6] Tumor heterogeneity, genetic mutations, multi drug resistance, and compromised immune responses contribute to inconsistent efficacy and complications such as recurrence and metastasis.[7–10] Consequently, there is a pressing need for more precise, personalized therapeutic approaches that can address these issues more effectively. Recent advances in nanotheranostics that combine diagnostic imaging with light-triggered therapy, offer promising alternatives to conventional treatments.[11–15] Nanotheranostics enables simultaneous localization of lesions and real-time monitoring of therapeutic effects, enhancing both diagnostic accuracy and therapeutic precision when combined with a nanoparticle system.[14,16] Traditional imaging modalities, such as computed tomography, magnetic resonance imaging, and positron emission tomography have their limitations, including inadequate sensitivity, low resolution, poor signal-to-background ratio, and high costs.[17–19] In contrast, fluorescence imaging (FLI) in the near-infrared (NIR) II window (1,000–1,700 nm) has demonstrated superior performance due to its high sensitivity, excellent spatial and temporal resolution, and deeper tissue penetration.[18,20] This is largely due to reduced tissue absorption and scattering, as well as lower autofluorescence compared to visible light and NIR-I imaging.[21] Among the promising NIR-II fluorophores, the organic dye IR1061 stands out for its high-resolution imaging capabilities and deep tissue penetration.[22–26] However, its clinical application has been limited by its low water solubility and short circulation time, which hinders its effectiveness in biological systems.[24,27] To overcome these limitations, integrating IR1061 into a nanoparticle (NPs) system could enhance its solubility, stability, and therapeutic efficacy.[23,27,28]

Hydroxyapatite (HAP), the principal inorganic component of human bone,[29] presents an attractive option as a nanoparticle platform for cancer therapy due to its biocompatibility and potential for selective tumor inhibition.[30–32] At the nanoscale, HAPs exhibits unique properties that improve its antitumor activity while minimizing impact on normal cells.[33–35] This is attributed to its size, morphology, dispersibility, and stability, which are critical for its effectiveness.[35] Despite these advantages, challenges such as HAPs tendency to agglomerate[36] and targeting have constraints its broader application in cancer therapy.[31] Recent reports claims that, < 1% of intravenously administered NPs accumulate in solid tumors.[37] This is due, in large part, to serum protein adsorption to the surface of nanocarriers while in circulation.[37,38] Besides destabilizing nanocarriers, adsorbed serum proteins trigger an immune response that leads to rapid blood clearance, all of which hinders accumulation in tumors.[38] Finally, for the small fraction of

nanocarriers that does reach the target tumor tissue, uptake into cancer cells represents a major challenge.[37,38]

This study, addresses these challenges by developing a multifunctional nanoparticle system that integrates the NIR-II IR1061 dye with a HAP nanoparticle (HAPNIRs). IR1061 dye encapsulated within HAPNs is wrapped with a lipid/PEG bilayer and functionalized with an acidity-triggered rational membrane (ATRAM) peptide to enhance tumor targeting and internalization (Figure 1). The ATRAM peptide facilitates specific binding and uptake by tumor cells in the acidic microenvironment typical of many cancers.[38–41] Additionally, the NIR-II IR1061 dye within the HAPNs is utilized for photothermal therapy (PTT). By converting light energy into localized heat, IR1061 facilitates the ablation of tumor tissues and enables real-time monitoring through fluorescence imaging.[23,27,42] This combination of technologies allows for a more precise and effective treatment modality. This NPs system not only improves the imaging capabilities and therapeutic outcomes of IR1061 but also enhances the stability and solubility of the dye. The integration of photothermal therapy with NIR-II imaging offers a synergistic approach to cancer treatment, enabling both effective lesion detection and targeted thermal ablation of tumors.[43] This approach holds significant promise for advancing cancer therapy by providing a non-invasive, high-resolution diagnostic tool and a potent therapeutic strategy in a single, integrated system.

RESULTS AND DISCUSSION

Preparation and Characterization of Hydroxyapatite Nanoparticles (HAPNs) and Lipid/PEG Coated HAPNs (LHAPNs)

A commonly used technique was used to synthesize the spherical shaped hydroxyapatite nanoparticles (HAPNs). This method employs a precise molecular-level mixing of calcium and phosphorous precursors, to achieve the chemical homogeneity.[44] Characterization of the synthesized HAPNs was conducted using the X-ray diffraction (XRD, Supporting Figure 1a). XRD patterns display a typical characteristic peak at (002), (211), (202), (310) and (004) and consistent with previously published reports.[45] The adsorption-desorption isotherms showed that the HAPNs has a specific surface area of ~23 m^2/g and an average pore diameter of ~1 nm (Supporting Figure 1b), aligning within the range reported for other types of promising HAPNs drug delivery platforms.[46] The composition of the HAPNs was validated by energy-dispersive X-ray spectroscopy (EDX) (Supporting Figure 1c; Supporting Figure 2a).[46] Imaging the HAPNs through transmission electron microscopy (TEM) imaging confirmed that the synthesized HAPNs have a uniformly spherical-like shape morphology (Figure 2a). For enhancing drug delivery capabilities, nanocarriers are often coated with lipid bilayer to boost their biocompatibility, stability in colloidal form, and enable controlled release of therapeutic agents.[45,46] These lipid layers facilitate easy functionalization, allowing for targeted delivery to specific tissues and cells.[48,49] Moreover, incorporating inert, water-soluble polymers like polyethylene glycol (PEG) into lipid bilayer reduce aggregation and minimize interactions with serum proteins, which are known to promote facilitate phagocytic clearance.[50] We followed established protocols to coat the surface of HAPNs with a bilayer of DPPC, cholesterol, and DSPE-PEG_{2000}-maleimide (Figure 2b–d; Supporting Figure 2b).[47,50] The interactions between the bilayer and the HAPNs are expected to be stabilized by van der Waals forces and electrostatic attractions between the phospholipid headgroups and the negatively charged HAPNs.[51] This bilayer composition (DPPC/cholesterol/DSPE-PEG_{2000}-maleimide in a 77.5:20:2.5 molar ratio) was selected based on our recent findings and previous studies.[41,47,52] This formulation is known to provide high colloidal stability, effective cargo loading, minimal baseline leakage and increasing the *in vivo* circulation half-life of the NPs.[41,47,52] Consistent with previous findings,[41,47] transmission electron microscopy (TEM) and scanning transmission electron microscopy (STEM) images demonstrated the presence of lipid/PEG layers on the surface of HAPNs (LHAPNs) (Figure 2b–d). The uniform coating of these lipid/PEG layers was further validated using cryo-mode TEM imaging (Supporting Figure 2b). This coating was further confirmed by dynamic light scattering (DLS). The LHAPNs exhibited a larger hydrodynamic diameter (~89 nm) compared to the uncoated HAPNs (~78 nm) (Figure 2e; Supporting Table 1), indicating a lipid/PEG bilayer coat thickness of ~5 nm at each

end of the NPs. Additionally, the zeta potential shifted from -6.5 mV to -13 mV following lipid/PEG coating (Figure 2f; Supporting Table 1), consistent with values reported for other lipid-coated NPs.

The colloidal stability of LHAPNs was evaluated to assess their suitability for tumor targeting and cancer therapy applications.[41,47,53,54] The hydrodynamic diameter of the NPs remained consistent over a 72 h period, with a value of 89 ± 8 nm in 10 mM phosphate buffer pH 7.4, 88 ± 9 nm in 50 mM sodium acetate buffer at pH 5.5, and 91.5 ± 1.5 nm in complete cell culture medium (RPMI 1640, 10% FBS, pH 7.4) over a 72 h period (Figure 2g–i). Notably, long-term monitoring demonstrated that LHAPNs maintained stability for at least a month in complete medium (~91 nm, Figure 2i). These findings suggest that lipid/PEG coating enhances colloidal stability, prevents serum protein adsorption, and allows the NPs to maintain an optimal size during *in vivo* circulation, which may facilitate tumor localization and internalization into cancer cells.[55,56]

Formation of a serum protein corona during circulation can destabilize nanocarriers, trigger immune responses, and lead to rapid clearance, thus impeding accumulation in target tumor tissues.[57] To address this, we analyzed serum protein desorption from the surface of the nanospheres using quantitative proteomics (Supporting Figure 3; Supporting Table 2). After incubating HAPNs and LHAPNs in complete cell culture medium for 72 h, we isolated the adsorbed serum proteins and quantified them using reversed-phase liquid chromatography-tandem mass spectrometry (RPLC-MS/MS) with label-free quantification (LFQ). Analysis of the 183 most abundant serum proteins, selected after filtering the unavoidable mass spectrometric contaminants, revealed substantially higher adsorption to the HAPNs compared to the LHAPNs (Supporting Figure 3b). These results confirm that the Lipid/PEG shell successfully minimizes the formation of a serum protein corona on the surface of LHAPNs.

Photothermal properties of IR1061-Loaded LHAPs (LHAPNIRs)

Recent studies have highlighted that laser operating within the second near-infrared window (NIR-II), with wavelengths from 1000 to 1350 nm, offer several advantages over NIR-I lasers.[58,59] NIR-II lasers demonstrate reduced absorption and scattering in biological tissues, leading to enhanced penetration and a higher energy safety threshold. For instance, the maximum permissible energy density for an NIR-II laser is 1 W/cm², compared to just 0.33 W/cm² for NIR-I lasers.[60] This makes NIR-II PTT a significant advancement for improving clinical safety and effectiveness. The IR1061 dye (Figure 1) is a commercial compound known for its strong absorption in the NIR-II range (with a maximum absorbance at 1064 nm) range and its high fluorescence quantum yield.[27,61,62] This makes it a promising candidate for NIR-II photothermal applications. Therefore, the photothermal agent IR1061 (Figure 1; Figure 2j) was encapsulated within the pores of the HAPNs (HAPNIRs) using a passive entrapment loading technique.[63] By

adjusting the feeding ratio, a relatively high loading capacity of IR1061 in the HAPNIRs was achieved (15 wt %, Supporting Table 3). For photothermal capability studies, we investigated the temperature changes induced by NIR-II laser illumination of the IR1061 loaded LHAPNs (LHAPNIRs) in aqueous solution.

As expected, no change in temperature was observed in LHAPNIRs in the absence of NIR light (Figure 3a–g). However, upon exposure to 980 nm laser light, the LHAPNIRs showed a robust, concentration and irradiation power density dependent, photothermal response (Figure 3a–f). For instance, at 100 µg/mL LHAPNIRs with 1.0 W/cm^2 irradiation for 5 min the temperature increased from 28.4 ± 2.1 to 43.5 ± 1.1 °C, while at 150 µg/mL LHAPNIRs with 1.5 W/cm^2 irradiation for 5 min the temperature rose to 55.7 ± 3.7 °C (Figure 3d,e), This suggests that the NPs loaded IR1061 can rapidly and efficiently convert NIR laser into heat of a temperature that is high enough to ablate the cancer cells (typically ~50 °C).[64] Notably, even with low power densities.[41,65] LHAPNIRs yielded significant temperature increases (e.g. at a concentration of 150 µg/mL, the temperature increased to 42.1 ± 2.6 °C at 1.5 W/cm^2 irradiation for 5 min, Figure 3f). This data is comparable to the responses reported for IR1061 loaded NPs that exhibit high photothermal conversion efficiencies.[24,42] In contrast, a negligible increase in temperature was recorded in the free IR1061 sample in saline compared to LHAPNIRs under the same experimental conditions (Figure 3f,g) due to the hydrophobicity of IR1061,[27] while in presence of the methanol, the temperature increased to 39.8 ± 2.6 °C. Additionally, the photothermal stability of LHAPNIRs was assessed over five laser on/off cycles. The maximum temperature (~55 °C) was nearly identical over the five successive heating/cooling cycles, underlining the high photostability of the LHAPNIRs (Figure 3h). Additionally, the photothermal response profile of LHAPNIRs matches that of other PTT nanomaterials.[66] Together, these results emphasize the PTT potential of the designed NPs.

Cancer cell uptake of ATRAM-functionalized Rhodamine-B-Loaded LHAPNs (ALHAPNRhBs)

For tumor targeting, Rhodamine B-loaded LHAPNs (LHAPNRhBs) were modified with the pH-responsive acidity-triggered rational membrane (ATRAM) peptide.[39] The interaction between ATRAM (N_t-CGLAGLAGLLGLEGLLGLPLGLLEGLWLGLELEGN-C_t) and cellular membranes is highly dependent on pH levels. At physiological pH, ATRAM remains largely unstructured and binds weakly and superficially to membranes. However, in acidic conditions, the peptide transitions to a transmembrane α-helical conformation within lipid bilayers (Figure 1b).[39–41] This transition to membrane insertion at lower pH is driven by increased hydrophobicity resulting from protonation of its glutamate residues.[39] Notably, the peptide's membrane insertion pKa is 6.5,[39] making ATRAM particularly effective for targeting cancer cells in the mildly acidic

environment (pH approximately 6.5–6.8) commonly found in solid tumors (Figure 1c). The zeta potential of ALHAPNs (~ -11mV) falls within the range reported for other highly stable nanocarriers at physiological pH.[41,67] Changing the pH to 6.5, the zeta potential of ALHAPNs increased to +11 mV, without adversely affecting the long-term colloidal stability of the NPs (Figure 2k; Supporting Table 1). These results suggest that ALHAPNs would effectively target tumor cells.

The pH-dependent uptake of ALHAPNRhBs in cancer cells was assessed using confocal fluorescence microscopy and flow cytometry. Human pancreatic cancer cells MIA PaCa-2 cell line were treated with ALHAPNRhBs for 4 h (Figure 4a–g). In Figure 4a, confocal microscopy images shows pH dependent targeted cellular internalization, and cytosolic localization, of ALHAPNRhBs under acidic conditions compared to physiological pH. Further, in Figure 4b–d, imaging results were confirmed using flow cytometry analysis, which shows impactful increase of ~9-fold higher uptake of ALHAPNRhBs was observed in MIA PaCa-2 cells at acidic pH 6.5 and incubation time (4 h). These results confirm that ATRAM facilitates uptake of ALHAPNRhBs specifically in cells within a mildly acidic environment.

We conducted a series of experiments to investigate the mechanisms of cellular internalization for ALHAPNRhBs. Depleting intracellular ATP with sodium azide and deoxyglucose resulted in only a partial reduction (about 50% of the control levels) in the uptake of ALHAPNRhBs. This suggests that the NPs are internalized through both energy-dependent (endocytosis) and energy-independent (direct translocation) pathways (Figure 4e–g). The direct translocation likely involves ATRAM-mediated anchoring, followed by the fusion of the lipid-based coating with the cancer cell membrane, resulting in the release of HAP into the cytoplasm. To further elucidate the nature of the energy-dependent pathway, we pretreated cells with specific inhibitors of endocytosis: chlorpromazine (which inhibits clathrin-coated pit formation), methyl-β-cyclodextrin (which disrupts lipid raft-mediated endocytic pathways by depleting cholesterol from the plasma membrane), filipin (an inhibitor of caveolae-dependent endocytosis), and amiloride (which blocks micropinocytosis by inhibiting Na^+/H^+ exchange).[68–70] Among all the inhibitors tested, only chlorpromazine significantly reduced the cellular uptake of ALHAPNRhBs, indicating that clathrin-mediated endocytosis plays a key role in this process (Figure 4e–g).

In cases of membrane translocation, ALHAPNRhBs would directly penetrate the cytosol. Conversely, after clathrin-mediated endocytosis, the acidification of the mature endocytic compartment would facilitate the insertion and disruption of the endosomal membrane by ATRAM, akin to the behaviour of other pH-responsive peptides, leading to the cytosolic release of ALHAPNRhBs. Thus, the pH-dependent uptake of ALHAPNRhBs occurs through multiple mechanisms, allowing the nanoparticles to efficiently penetrate tumor cells.

Cytotoxicity of ALHAPNIRs

The cytotoxicity of the designed NPs against the MIA PaCa-2 cancer cells was evaluated using the MTS cell viability assay. Treatment with IR1061-free LHAPNs (5–150 μg/mL) did not reduce MIA PaCa-2 cell viability regardless of laser irradiation (Supporting Figure 4a). Likewise, without NIR laser light the LHAPNIRs were not toxic to MIA PaCa-2 cells, up to a IR1061 concentration of 5 μg/mL, either at physiological or acidic pH (pH 7.4 or 6.5) (Supporting Figure 4b). These results confirm that the NPs are biocompatible and therefore suitable for pH-responsive photothermal cancer therapy applications.

In the presence of 980 nm laser light, treatment with ALHAPNIRs over the periods ranging from 24–72 h revealed no detrimental effects on the viability of MIA PaCa-2 cells when incubated at a physiological pH of 7.4. Initially, cells were incubated with ALHAPNIRs at IR1061 concentration of 0–5 μg/mL for 6 h, after which media was replaced. Subsequently, cells were subjected to laser irradiation at varying laser power densities (0.4, 1.0 or 1.5 W/cm^2) for 3- or 5-min (Figure 5a–f and Supporting Figure 5,6). The data indicated that the poor internalization of the NPs at physiological pH was likely the cause for the lack of toxicity. Conversely, when the MIA PaCa-2 cells were exposed to ALHAPNIRs at a pH of 6.5, a significant reduction in cell viability was observed (Figure 5a–f). The cytotoxic effects of the NPs were directly correlated with the concentration and irradiation power and duration. The data suggest a clear relationship between these factors and the extent of cell death, as depicted in Figures 5a–f**.**

Notably, at pH 6.5, the viability of MIA PaCa-2 cells displayed a dependency on the concentration of ALHAPNIRs, the duration of incubation, and the power density applied. This dependence was evident over both 24 h (Supporting Figure 5) and 72 h (Supporting Figure 6) treatment periods, underscoring the potential of ALHAPNIRs as a targeted therapeutic strategy. These findings highlight the critical role of pH in mediating the efficacy of ALHAPNIRs. The MTS assay results were supported by a confocal live/dead cell assay (Figure 6a), with calcein AM/propidium iodide (PI) staining, which showed that treatment of the cells with ALHAPNIRs at pH 6.5 in combination with 980 nm laser irradiations resulted in cell toxicity (Figure 6b,c). Combined with the cell uptake experiments, the cell viability assays confirm that ATRAM is required for both the pH-dependent cancer cell uptake and the associated NIR light-induced cytotoxicity of the NPs. In addition to MTS and calcein AM/propidium iodide (PI) staining, we then investigated the LDH cell release as a proxy for cell death (Figure 6d,e).[71] Consistent with the previous cell viability analysis results, we observed that ALHAPNIRs caused significant LDH release after 3- and 5-min irradiation.

Macrophage Recognition and Immunogenicity of ALHAPNIRs

The opsonization of NPs and their subsequent uptake by monocytes and macrophages of the mononuclear phagocyte system results in the accumulation of NPs in healthy organs like the spleen and liver, rather than in target solid tumors or tumor-associated macrophages.[72] To address this challenge, NPs are often coated with neutral molecules, such as PEG, which are known to reduce protein adsorption and MPS-mediated clearance.[56] Nevertheless, research has shown that surface modification with substances like PEG can sometimes provoke immune responses.[73]

Exposure to HAPNIRs reduced viability of THP-1 cells, and induced production of the inflammatory cytokines tumor necrosis factor-alpha (TNF-α) and interlukin 1 beta (Il-1β), by the macrophages (Supporting Figure 7a,b). In contrast, no significant toxicity or TNF-α/ Il-1β production was observed following treatment with ALHAPNIRs (Supporting Figure 7a,b). These results demonstrate that ALHAPNIRs effectively escape recognition and uptake by macrophages, a property of the lipid/PEG-coated nanospheres that is critical for their capacity to effectively target tumors.

Biodistribution of DiD- or IR1061-loaded ALHAPNs (ALHAPNDiDs or ALHAPNIRs)

Encouraged by the effective *in vitro* internalization of ALHAPRhBs by MIA PaCa-2 cancer cells, we then studied the *in vivo* tumor localization of the ALHAPNDiDs or ALHAPNIRs in MIA PaCa-2 tumor implanted mice using the IVIS optical and thermal imaging. Following intravenous injection of the saline or lipophilic near-infrared (NIR) dye DiD, encapsulated NPs (HAPNDiDs or LHAPNDiDs or ALHAPNDiDs) in the MIA PaCa-2 tumor-bearing mice, the fluorescence images were captured using the IVIS Spectrum with a spectrum unmixing approach. Images were acquired with an excitation and emission set at 605 nm and 640 nm and an emission range of 640 to 720 nm at varying time points of 0, 2, 4, 8, 24, 48 and 72 h (Figure 7a). The MIA PaCa-2 tumors in the ALHAPNDiDs treated group showed a much higher tumor localization compared to those with HAPNDiDs and LHAPNDiDs (Figure 7a,b). The DiD fluorescence intensity in the ALHAPNDiDs from MIA PaCa-2 tumors was ten times higher than that of the saline or HAPNDiDs or LHAPNDiDs injected groups (Figure 7b). Seventy-two hours after *i.v.* injection of the NPs, the tumors and vital organs (lungs, liver, spleen, kidney and heart) from different groups were collected for *ex vivo* fluorescence imaging (Figure 7c). The DiD fluorescence intensity in MIA PaCa-2 tumors treated with ALHAPNDiDs was ~3 times higher when compared to saline or HAPNDiDs or LHAPNDiDs NPs (Figure 7c). Moreover, DiD fluorescence signal in vital organs was low in ALHAPNDiDs mice, confirming the biocompatibility of the NPs. Similarly, thermal imaging following 980 nm laser irradiation (1.0 W/cm^2) showed that ALHAPNIRs induced a much more rapid and pronounced temperature

increase in the tumors (from 36 to 55 °C within 5 min) compared to the HAPNIRs and LHAPNIRs (Supporting Figure 8). Indeed, the photothermal response of the ALHAPNIRs is comparable to that of other highly effective PTT nanomaterials,[74,75] which underscore the high *in vivo* photothermal conversion efficiency and photostability of ALHAPNIRs. Taken together, these results illustrate that ALHAPNs effectively target tumors and facilitate multimodal – fluorescence and thermal – imaging of the cancerous tissue.

In vivo Tumor Growth Inhibition by ALHAPNIRs

Based on the encouraging *in vitro* findings demonstrating potent and selective anticancer activity of ALHAPNIRs under NIR light (Figure 4–6), alongside their minimal interactions with serum proteins and macrophages (Supporting Figure 3), we proceeded to assess the antitumor efficacy of these NPs *in vivo*.

Mice with subcutaneous MIA PaCa-2 tumors (Figure 8a,b) were administered intravenous injections of saline, HAPs or LHAPNIRs or ALHAPNIRs (22 mg/kg NPs, 3.3 mg/kg IR1061), every 2 days for a total of 15 doses (Figure 8a). The dosage of IR1061 injected was comparable to that used in other PTT-based cancer treatment studies.[76] As anticipated, in the absence of 980 nm laser irradiation, none of the treatments significantly affected body weight, tumor growth or overall survival of the mice (Figure 8c,d,i). In the presence of NIR laser irradiation, HAPNIRs demonstrated minimal anticancer effects, with only a modest enhancement observed upon loading the NPs with IR1061 (Figure 8e). In contrast, the ALHAPNIRs treatment resulted in a more substantial inhibition of tumor growth (Figure 8e) and a notable extension of median survival time (Figure 8i). Indeed, the ALHAPNIRs treatment group exhibited the most pronounced antitumor effects, reducing the initial tumor volume from 25.95 ± 0.975 mm^3 to 21.93 ± 1.95 mm^3 (Figure 8e) and decreasing the tumor mass to approximately 3.7% of the control levels (Figures 8f,g). Furthermore, ALHAPNIRs significantly prolonged survival compared to controls and all other treatment groups throughout the duration of the experiment (Figure 8i). Histological analysis using hematoxylin and eosin (H&E) staining corroborated the superior antitumor efficacy of ALHAPNIRs relative to other treatments (Figure 8j). Importantly, treatment with ALHAPNIRs, both with and without NIR irradiation, did not adversely affect the body weight of the mice (Figure 8c), and no abnormalities or lesions were detected in H&E-stained sections of vital organs, including the heart, kidney, liver, lung, and spleen (Supporting Figure 9). Additionally, exposure to ALHAPNIRs, did not significantly increased the concentrations of inflammatory cytokines, TNF-α and Il-1β, in circulation (Supporting Figure 10). Collectively, these *in vitro* and *in vivo* findings compellingly demonstrate that IR1061-loaded ALHAPNs effectively reduce tumor size through NIR-induced PTT, while safeguarding healthy tissue and significantly enhancing survival outcomes.

CONCLUSIONS

Photothermal therapy (PTT) shows significant promise as a non-invasive, light-based approach to cancer treatment.[43,76,77] However, several challenges have hindered its widespread clinical application. Key issues include insufficient solubility, low stability, and a lack of specificity for tumor cells in many commonly used photothermal agents. In this study, we introduced a simple and robust solution: ATRAM-functionalized, lipid-coated ALHAPNIRs that address these challenges and exhibit several critical properties. First, these NPs demonstrate high stability for the PTAs, ensuring effective delivery and prolonged therapeutic action. Second, they exhibit minimal interactions with healthy tissues, serum proteins, and macrophages, which significantly increases the *in vivo* circulation of the PTA cargo. This extended circulation time enhances the potential for targeting cancer cells effectively. Moreover, these ALHAPNIRs facilitate efficient and specific internalization into cancer cells, particularly in the mildly acidic microenvironment characteristic of solid tumors. This targeted uptake is crucial for maximizing therapeutic efficacy while minimizing damage to surrounding healthy tissue. Additionally, the NPs are excited by NIR light, which offers superior tissue penetration, lower autofluorescence, and reduced phototoxicity compared to visible light. Collectively, these features underscore the potential of biocompatible and biodegradable ALHAPNIRs as a promising nanoplatform that not only enables targeted tumor therapy but also integrates diagnostic imaging capabilities. This dual functionality could pave the way for more effective and safer cancer treatment strategies in the future.

ACKNOWLEDGEMENTS

The authors express their gratitude to Ms. Jumaanah Alhashemi, Assistant Director of Research Visualization and Fabrication Services at NYU Abu Dhabi, for creating the graphic illustrations. They also acknowledge the NYU Abu Dhabi Center for Genomics and Systems Biology (NYUAD-CGSB) for granting access to the BD FACSAria III for flow cytometry measurements. Imaging – confocal fluorescence microscopy, TEM, and IVIS Spectrum – and Zetasizer measurements, were conducted using the Core Technology Platforms (CTP) at NYU Abu Dhabi. Additionally, proteomics data processing utilized the High-Performance Computing (HPC) resources at the same institution. This research was funded by a research NYU Abu Dhabi (AD389) for M.M. and a research grant from the U.S. National Institutes of Health (R35GM140846) for F.N.B.

SUPPORTING INFORMATION

Supporting Figures: characterization of the hydroxyapatite nanoparticles (HAPNs); characterization of the HAPNs and LHAPNs; quantitative proteomics analysis of serum protein adsorption to the surface of HAPNs and LHAPNs; cytotoxicity of the nanoparticles in the absence of NIR laser irradiation; MTS cell viability measurements for 24 h following NIR laser irradiation; MTS cell viability measurements for 72 h following NIR laser irradiation; macrophage recognition and immunogenicity of the nanoparticles; thermal imaging of MIA PaCa-2 tumor-bearing mice upon NIR laser irradiation; histological analysis of vital organs following treatment with the nanospheres; quantification of cytokines in the serum of test mice. **Supporting Tables**: summary of hydrodynamic diameters and zeta potentials of HAPNs, LHAPNs and ALHAPNs; IR1061 loading capacity of the HAPNs; proteins corresponding to the UniProt Knowledgebase (UniProtKB) accession numbers shown in Supporting Figure 3. **Supporting Experimental Section**: reagents; synthesis of the HAPNs; synthesis of HAPNIRs; synthesis of Lipid/PEG-Coated HAPNs (LHAPNs); Synthesis of ATRAM-functionalized LHAPNs (ALHAPNs); Characterization of the nanoparticles; photothermal response;quantitative proteomic analysis; cell culture; cancer cell uptake of ALHAPNRhBs; cell viability/toxicity assays;macrophage toxicity and immunogenicity; biodistribution *in vivo*; cytokines in the serum; tumor growth inhibition studies; histological analyses.

COMPETING INTERESTS

The authors declare no competing financial interests.

REFERENCES

(1) Zitvogel, L.; Apetoh, L.; Ghiringhelli, F.; Kroemer, G. Immunological Aspects of Cancer Chemotherapy. *Nat Rev Immunol* **2008**, *8* (1), 59–73. https://doi.org/10.1038/nri2216.

(2) Mellman, I.; Coukos, G.; Dranoff, G. Cancer Immunotherapy Comes of Age. *Nature* **2011**, *480* (7378), 480–489. https://doi.org/10.1038/nature10673.

(3) Khalil, D. N.; Smith, E. L.; Brentjens, R. J.; Wolchok, J. D. The Future of Cancer Treatment: Immunomodulation, CARs and Combination Immunotherapy. *Nat Rev Clin Oncol* **2016**, *13* (5), 273–290. https://doi.org/10.1038/nrclinonc.2016.25.

(4) Holohan, C.; Van Schaeybroeck, S.; Longley, D. B.; Johnston, P. G. Cancer Drug Resistance: An Evolving Paradigm. *Nat Rev Cancer* **2013**, *13* (10), 714–726. https://doi.org/10.1038/nrc3599.

(5) Housman, G.; Byler, S.; Heerboth, S.; Lapinska, K.; Longacre, M.; Snyder, N.; Sarkar, S. Drug Resistance in Cancer: An Overview. *Cancers (Basel)* **2014**, *6* (3), 1769–1792. https://doi.org/10.3390/cancers6031769.

(6) Hanahan, D.; Weinberg, R. A. Hallmarks of Cancer: The next Generation. *Cell* **2011**, *144* (5), 646–674. https://doi.org/10.1016/j.cell.2011.02.013.

(7) Sun, X.; Yu, Q. Intra-Tumor Heterogeneity of Cancer Cells and Its Implications for Cancer Treatment. *Acta Pharmacol Sin* **2015**, *36* (10), 1219–1227. https://doi.org/10.1038/aps.2015.92.

(8) Janssen, L. M. E.; Ramsay, E. E.; Logsdon, C. D.; Overwijk, W. W. The Immune System in Cancer Metastasis: Friend or Foe? *J Immunother Cancer* **2017**, *5* (1), 79. https://doi.org/10.1186/s40425-017-0283-9.

(9) Wang, X.; Zhang, H.; Chen, X. Drug Resistance and Combating Drug Resistance in Cancer. *Cancer Drug Resist* **2019**, *2* (2), 141–160. https://doi.org/10.20517/cdr.2019.10.

(10) Marusyk, A.; Janiszewska, M.; Polyak, K. Intratumor Heterogeneity: The Rosetta Stone of Therapy Resistance. *Cancer cell* **2020**, *37* (4), 471. https://doi.org/10.1016/j.ccell.2020.03.007.

(11) Kim, J.; Piao, Y.; Hyeon, T. Multifunctional Nanostructured Materials for Multimodal Imaging, and Simultaneous Imaging and Therapy. *Chem. Soc. Rev.* **2009**, *38* (2), 372–390. https://doi.org/10.1039/B709883A.

(12) Park, S.; Aalipour, A.; Vermesh, O.; Yu, J. H.; Gambhir, S. S. Towards Clinically Translatable in Vivo Nanodiagnostics. *Nat Rev Mater* **2017**, *2* (5), 1–20. https://doi.org/10.1038/natrevmats.2017.14.

(13) Wang, Z.; Zhen, X.; Upputuri, P. K.; Jiang, Y.; Lau, J.; Pramanik, M.; Pu, K.; Xing, B. Redox-Activatable and Acid-Enhanced Nanotheranostics for Second Near-Infrared Photoacoustic Tomography and Combined Photothermal Tumor Therapy. *ACS Nano* **2019**, *13* (5), 5816–5825. https://doi.org/10.1021/acsnano.9b01411.

(14) Overchuk, M.; Weersink, R. A.; Wilson, B. C.; Zheng, G. Photodynamic and Photothermal Therapies: Synergy Opportunities for Nanomedicine. *ACS Nano* **2023**, *17* (9), 7979–8003. https://doi.org/10.1021/acsnano.3c00891.

(15) Fan, D.; Cao, Y.; Cao, M.; Wang, Y.; Cao, Y.; Gong, T. Nanomedicine in Cancer Therapy. *Sig Transduct Target Ther* **2023**, *8* (1), 1–34. https://doi.org/10.1038/s41392-023-01536-y.

(16) Sun, L.; Liu, H.; Ye, Y.; Lei, Y.; Islam, R.; Tan, S.; Tong, R.; Miao, Y.-B.; Cai, L. Smart Nanoparticles for Cancer Therapy. *Sig Transduct Target Ther* **2023**, *8* (1), 1–28. https://doi.org/10.1038/s41392-023-01642-x.

(17) Ntziachristos, V.; Ripoll, J.; Wang, L. V.; Weissleder, R. Looking and Listening to Light: The Evolution of Whole-Body Photonic Imaging. *Nat Biotechnol* **2005**, *23* (3), 313–320. https://doi.org/10.1038/nbt1074.

(18) Smith, A. M.; Mancini, M. C.; Nie, S. Second Window for in Vivo Imaging. *Nature Nanotech* **2009**, *4* (11), 710–711. https://doi.org/10.1038/nnano.2009.326.

(19) Naumova, A. V.; Modo, M.; Moore, A.; Murry, C. E.; Frank, J. A. Clinical Imaging in Regenerative Medicine. *Nat Biotechnol* **2014**, *32* (8), 804–818. https://doi.org/10.1038/nbt.2993.

(20) Hong, G.; Antaris, A. L.; Dai, H. Near-Infrared Fluorophores for Biomedical Imaging. *Nat Biomed Eng* **2017**, *1* (1), 1–22. https://doi.org/10.1038/s41551-016-0010.

(21) Li, Y.; Qi, H.; Geng, Y.; Li, L.; Cai, X. Research Progress of Organic Photothermal Agents Delivery and Synergistic Therapy Systems. *Colloids and Surfaces B: Biointerfaces* **2024**, *234*, 113743. https://doi.org/10.1016/j.colsurfb.2024.113743.

(22) Casalboni, M.; De Matteis, F.; Prosposito, P.; Quatela, A.; Sarcinelli, F. Fluorescence Efficiency of Four Infrared Polymethine Dyes. *Chemical Physics Letters* **2003**, *373* (3), 372–378. https://doi.org/10.1016/S0009-2614(03)00608-0.

(23) Tao, Z.; Hong, G.; Shinji, C.; Chen, C.; Diao, S.; Antaris, A. L.; Zhang, B.; Zou, Y.; Dai, H. Biological Imaging Using Nanoparticles of Small Organic Molecules with Fluorescence Emission at Wavelengths Longer than 1000 Nm. *Angewandte Chemie International Edition* **2013**, *52* (49), 13002–13006. https://doi.org/10.1002/anie.201307346.

(24) Du, B.; Liu, R.; Qu, C.; Qian, K.; Suo, Y.; Wu, F.; Chen, H.; Li, X.; Li, Y.; Liu, H.; Cheng, Z. J-Aggregates Albumin-Based NIR-II Fluorescent Dye Nanoparticles for Cancer Phototheranostics. *Materials Today Bio* **2022**, *16*, 100366. https://doi.org/10.1016/j.mtbio.2022.100366.

(25) Umezawa, M.; Kobayashi, H.; Ichihashi, K.; Sekiyama, S.; Okubo, K.; Kamimura, M.; Soga, K. Heat Treatment Effects for Controlling Dye Molecular States in the Hydrophobic Core of Over-1000 Nm Near-Infrared (NIR-II) Fluorescent Micellar Nanoparticles. *ACS Omega* **2022**, *7* (7), 5817–5824. https://doi.org/10.1021/acsomega.1c05771.

(26) Huang, Y.; Wei, D.; Wang, B.; Tang, D.; Cheng, A.; Xiao, S.; Yu, Y.; Huang, W. NIR-II Light Evokes DNA Cross-Linking for Chemotherapy and Immunogenic Cell Death. *Acta Biomaterialia* **2023**, *160*, 198–210. https://doi.org/10.1016/j.actbio.2023.02.012.

(27) Chen, Q.; Chen, J.; He, M.; Bai, Y.; Yan, H.; Zeng, N.; Liu, F.; Wen, S.; Song, L.; Sheng, Z.; Liu, C.; Fang, C. Novel Small Molecular Dye-Loaded Lipid Nanoparticles with Efficient near-Infrared-II Absorption for Photoacoustic Imaging and Photothermal Therapy of Hepatocellular Carcinoma. *Biomater. Sci.* **2019**, *7* (8), 3165–3177. https://doi.org/10.1039/C9BM00528E.

(28) Kamimura, M.; Takahiro, S.; Yoshida, M.; Hashimoto, Y.; Fukushima, R.; Soga, K. Over-1000 Nm near-Infrared Fluorescent Biodegradable Polymer Nanoparticles for Deep Tissue in Vivo Imaging in the Second Biological Window. *Polym J* **2017**, *49* (12), 799–803. https://doi.org/10.1038/pj.2017.59.

(29) Ginebra, M. P.; Traykova, T.; Planell, J. A. Calcium Phosphate Cements as Bone Drug Delivery Systems: A Review. *Journal of Controlled Release* **2006**, *113* (2), 102–110. https://doi.org/10.1016/j.jconrel.2006.04.007.

(30) Lin, K.; Chang, J. 1 - Structure and Properties of Hydroxyapatite for Biomedical Applications. In *Hydroxyapatite (Hap) for Biomedical Applications*; Mucalo, M., Ed.;

Woodhead Publishing Series in Biomaterials; Woodhead Publishing, 2015; pp 3–19. https://doi.org/10.1016/B978-1-78242-033-0.00001-8.

(31) Qian, G.; Xiong, L.; Ye, Q. Hydroxyapatite-Based Carriers for Tumor Targeting Therapy. *RSC Adv 13* (24), 16512–16528. https://doi.org/10.1039/d3ra01476b.

(32) Mondal, S.; Park, S.; Choi, J.; Vu, T. T. H.; Doan, V. H. M.; Vo, T. T.; Lee, B.; Oh, J. Hydroxyapatite: A Journey from Biomaterials to Advanced Functional Materials. *Advances in Colloid and Interface Science* **2023**, *321*, 103013. https://doi.org/10.1016/j.cis.2023.103013.

(33) Zhang, K.; Zhou, Y.; Xiao, C.; Zhao, W.; Wu, H.; Tang, J.; Li, Z.; Yu, S.; Li, X.; Min, L.; Yu, Z.; Wang, G.; Wang, L.; Zhang, K.; Yang, X.; Zhu, X.; Tu, C.; Zhang, X. Application of Hydroxyapatite Nanoparticles in Tumor-Associated Bone Segmental Defect. *Science Advances* **2019**, *5* (8), eaax6946. https://doi.org/10.1126/sciadv.aax6946.

(34) Lara-Ochoa, S.; Ortega-Lara, W.; Guerrero-Beltrán, C. E. Hydroxyapatite Nanoparticles in Drug Delivery: Physicochemistry and Applications. *Pharmaceutics* **2021**, *13* (10), 1642. https://doi.org/10.3390/pharmaceutics13101642.

(35) De Lama-Odría, M. del C.; del Valle, L. J.; Puiggalí, J. Hydroxyapatite Biobased Materials for Treatment and Diagnosis of Cancer. *Int J Mol Sci* **2022**, *23* (19), 11352. https://doi.org/10.3390/ijms231911352.

(36) Preparation of Hydroxyapatite Nanoparticle-Hyaluronic Acid Hybrid Membranes through Citric Acid Molecular Mediation. *Materials Advances* **2024**, *5* (5), 1887–1891. https://doi.org/10.1039/d3ma00882g.

(37) Wilhelm, S.; Tavares, A. J.; Dai, Q.; Ohta, S.; Audet, J.; Dvorak, H. F.; Chan, W. C. W. Analysis of Nanoparticle Delivery to Tumours. *Nat Rev Mater* **2016**, *1* (5), 1–12. https://doi.org/10.1038/natrevmats.2016.14.

(38) Palanikumar, L.; Al-Hosani, S.; Kalmouni, M.; Nguyen, V. P.; Ali, L.; Pasricha, R.; Barrera, F. N.; Magzoub, M. pH-Responsive High Stability Polymeric Nanoparticles for Targeted Delivery of Anticancer Therapeutics. *Communications Biology* **2020**, *3* (1), 1–17. https://doi.org/10.1038/s42003-020-0817-4.

(39) Nguyen, V. P.; Alves, D. S.; Scott, H. L.; Davis, F. L.; Barrera, F. N. A Novel Soluble Peptide with pH-Responsive Membrane Insertion. *Biochemistry* **2015**, *54* (43), 6567–6575. https://doi.org/10.1021/acs.biochem.5b00856.

(40) Nguyen, Vanessa. P.; Palanikumar, L.; Kennel, S. J.; Alves, D. S.; Ye, Y.; Wall, J. S.; Magzoub, M.; Barrera, F. N. Mechanistic Insights into the pH-Dependent Membrane Peptide ATRAM. *J Control Release* **2019**, *298*, 142–153. https://doi.org/10.1016/j.jconrel.2019.02.010.

(41) Palanikumar, L.; Kalmouni, M.; Houhou, T.; Abdullah, O.; Ali, L.; Pasricha, R.; Straubinger, R.; Thomas, S.; Afzal, A. J.; Barrera, F. N.; Magzoub, M. pH-Responsive Upconversion Mesoporous Silica Nanospheres for Combined Multimodal Diagnostic Imaging and Targeted Photodynamic and Photothermal Cancer Therapy. *ACS Nano* **2023**, *17* (19), 18979–18999. https://doi.org/10.1021/acsnano.3c04564.

(42) He, L.; Qing, F.; Li, M.; Lan, D. Paclitaxel/IR1061-Co-Loaded Protein Nanoparticle for Tumor-Targeted and pH/NIR-II-Triggered Synergistic Photothermal-Chemotherapy. *Int J Nanomedicine* **2020**, *15*, 2337–2349. https://doi.org/10.2147/IJN.S240707.

(43) Zhu, W.; Guo, Y.; Huang, J.; Zhang, Y.; Ni, Z.; Wei, M.; Liu, L.; Li, Y.; Zhang, M.; Tang, B. Z. NIR-II Photothermal Therapy Mediated by Polymer-Based Nanoparticles to Enhance Checkpoint Inhibitor Immunotherapy for Inhibiting Lymph Node Metastasis in Oral

Squamous Cell Carcinoma. *Nano Today* **2024**, *57*, 102351. https://doi.org/10.1016/j.nantod.2024.102351.

(44) Zhang, Y.; Lu, J. A Simple Method to Tailor Spherical Nanocrystal Hydroxyapatite at Low Temperature. *J Nanopart Res* **2007**, *9* (4), 589–594. https://doi.org/10.1007/s11051-006-9177-3.

(45) Mokhtar, M. Z.; Altujjar, A.; Wang, B.; Chen, Q.; Ke, J. C.-R.; Cai, R.; Zibouche, N.; Spencer, B. F.; Jacobs, J.; Thomas, A. G.; Hall, D.; Haigh, S. J.; Lewis, D. J.; Curry, R.; Islam, M. S.; Saunders, B. R. Spherical Hydroxyapatite Nanoparticle Scaffolds for Reduced Lead Release from Damaged Perovskite Solar Cells. *Commun Mater* **2022**, *3* (1), 1–12. https://doi.org/10.1038/s43246-022-00299-3.

(46) Safitri, N.; Rauf, N.; Tahir, D. Enhancing Drug Loading and Release with Hydroxyapatite Nanoparticles for Efficient Drug Delivery: A Review Synthesis Methods, Surface Ion Effects, and Clinical Prospects. *Journal of Drug Delivery Science and Technology* **2023**, *90*, 105092. https://doi.org/10.1016/j.jddst.2023.105092.

(47) Meng, H.; Wang, M.; Liu, H.; Liu, X.; Situ, A.; Wu, B.; Ji, Z.; Chang, C. H.; Nel, A. E. Use of a Lipid-Coated Mesoporous Silica Nanoparticle Platform for Synergistic Gemcitabine and Paclitaxel Delivery to Human Pancreatic Cancer in Mice. *ACS Nano* **2015**, *9* (4), 3540–3557. https://doi.org/10.1021/acsnano.5b00510.

(48) Butler, K. S.; Durfee, P. N.; Theron, C.; Ashley, C. E.; Carnes, E. C.; Brinker, C. J. Protocells: Modular Mesoporous Silica Nanoparticle-Supported Lipid Bilayers for Drug Delivery. *Small* **2016**, *12* (16), 2173–2185. https://doi.org/10.1002/smll.201502119.

(49) Riaz, M. K.; Riaz, M. A.; Zhang, X.; Lin, C.; Wong, K. H.; Chen, X.; Zhang, G.; Lu, A.; Yang, Z. Surface Functionalization and Targeting Strategies of Liposomes in Solid Tumor Therapy: A Review. *Int J Mol Sci* **2018**, *19* (1), 195. https://doi.org/10.3390/ijms19010195.

(50) Dai, Q.; Walkey, C.; Chan, W. C. W. Polyethylene Glycol Backfilling Mitigates the Negative Impact of the Protein Corona on Nanoparticle Cell Targeting. *Angewandte Chemie International Edition* **2014**, *53* (20), 5093–5096. https://doi.org/10.1002/anie.201309464.

(51) Liu, X.; Situ, A.; Kang, Y.; Villabroza, K. R.; Liao, Y.; Chang, C. H.; Donahue, T.; Nel, A. E.; Meng, H. Irinotecan Delivery by Lipid-Coated Mesoporous Silica Nanoparticles Shows Improved Efficacy and Safety over Liposomes for Pancreatic Cancer. *ACS Nano* **2016**, *10* (2), 2702–2715. https://doi.org/10.1021/acsnano.5b07781.

(52) LaBauve, A. E.; Rinker, T. E.; Noureddine, A.; Serda, R. E.; Howe, J. Y.; Sherman, M. B.; Rasley, A.; Brinker, C. J.; Sasaki, D. Y.; Negrete, O. A. Lipid-Coated Mesoporous Silica Nanoparticles for the Delivery of the ML336 Antiviral to Inhibit Encephalitic Alphavirus Infection. *Sci Rep* **2018**, *8* (1), 13990. https://doi.org/10.1038/s41598-018-32033-w.

(53) Moore, T. L.; Rodriguez-Lorenzo, L.; Hirsch, V.; Balog, S.; Urban, D.; Jud, C.; Rothen-Rutishauser, B.; Lattuada, M.; Petri-Fink, A. Nanoparticle Colloidal Stability in Cell Culture Media and Impact on Cellular Interactions. *Chem. Soc. Rev.* **2015**, *44* (17), 6287–6305. https://doi.org/10.1039/C4CS00487F.

(54) Placente, D.; Benedini, L. A.; Baldini, M.; Laiuppa, J. A.; Santillán, G. E.; Messina, P. V. Multi-Drug Delivery System Based on Lipid Membrane Mimetic Coated Nano-Hydroxyapatite Formulations. *International Journal of Pharmaceutics* **2018**, *548* (1), 559–570. https://doi.org/10.1016/j.ijpharm.2018.07.036.

(55) Tao, L.; Faig, A.; Uhrich, K. E. Liposomal Stabilization Using a Sugar-Based, PEGylated Amphiphilic Macromolecule. *Journal of Colloid and Interface Science* **2014**, *431*, 112–116. https://doi.org/10.1016/j.jcis.2014.06.004.

(56) Suk, J. S.; Xu, Q.; Kim, N.; Hanes, J.; Ensign, L. M. PEGylation as a Strategy for Improving Nanoparticle-Based Drug and Gene Delivery. *Adv Drug Deliv Rev* **2016**, *99* (Pt A), 28–51. https://doi.org/10.1016/j.addr.2015.09.012.

(57) Oh, J. Y.; Kim, H. S.; Palanikumar, L.; Go, E. M.; Jana, B.; Park, S. A.; Kim, H. Y.; Kim, K.; Seo, J. K.; Kwak, S. K.; Kim, C.; Kang, S.; Ryu, J.-H. Cloaking Nanoparticles with Protein Corona Shield for Targeted Drug Delivery. *Nature Communications* **2018**, *9* (1), 4548. https://doi.org/10.1038/s41467-018-06979-4.

(58) Vijayaraghavan, P.; Liu, C.-H.; Vankayala, R.; Chiang, C.-S.; Hwang, K. C. Designing Multi-Branched Gold Nanoechinus for NIR Light Activated Dual Modal Photodynamic and Photothermal Therapy in the Second Biological Window. *Advanced Materials* **2014**, *26* (39), 6689–6695. https://doi.org/10.1002/adma.201400703.

(59) Yang, T.; Tang, Y.; Liu, L.; Lv, X.; Wang, Q.; Ke, H.; Deng, Y.; Yang, H.; Yang, X.; Liu, G.; Zhao, Y.; Chen, H. Size-Dependent Ag2S Nanodots for Second Near-Infrared Fluorescence/Photoacoustics Imaging and Simultaneous Photothermal Therapy. *ACS Nano* **2017**, *11* (2), 1848–1857. https://doi.org/10.1021/acsnano.6b07866.

(60) Lu, W.; Melancon, M. P.; Xiong, C.; Huang, Q.; Elliott, A.; Song, S.; Zhang, R.; Flores, L. G., II; Gelovani, J. G.; Wang, L. V.; Ku, G.; Stafford, R. J.; Li, C. Effects of Photoacoustic Imaging and Photothermal Ablation Therapy Mediated by Targeted Hollow Gold Nanospheres in an Orthotopic Mouse Xenograft Model of Glioma. *Cancer Research* **2011**, *71* (19), 6116–6121. https://doi.org/10.1158/0008-5472.CAN-10-4557.

(61) Xie, X.; Hu, Y.; Zhang, C.; Song, J.; Zhuang, S.; Wang, Y. A Targeted Biocompatible Organic Nanoprobe for Photoacoustic and Near-Infrared-II Fluorescence Imaging in Living Mice. *RSC Adv.* **2018**, *9* (1), 301–306. https://doi.org/10.1039/C8RA08163H.

(62) Li, J.; Pu, K. Development of Organic Semiconducting Materials for Deep-Tissue Optical Imaging, Phototherapy and Photoactivation. *Chem. Soc. Rev.* **2019**, *48* (1), 38–71. https://doi.org/10.1039/C8CS00001H.

(63) Palanikumar, L.; Choi, E. S.; Oh, J. Y.; Park, S. A.; Choi, H.; Kim, K.; Kim, C.; Ryu, J.-H. Importance of Encapsulation Stability of Nanocarriers with High Drug Loading Capacity for Increasing in Vivo Therapeutic Efficacy. *Biomacromolecules* **2018**, *19* (7), 3030–3039. https://doi.org/10.1021/acs.biomac.8b00589.

(64) Li, X.; Lovell, J. F.; Yoon, J.; Chen, X. Clinical Development and Potential of Photothermal and Photodynamic Therapies for Cancer. *Nature Reviews Clinical Oncology* **2020**, *17* (11), 657–674. https://doi.org/10.1038/s41571-020-0410-2.

(65) Yuan, H.; Fales, A. M.; Vo-Dinh, T. TAT Peptide-Functionalized Gold Nanostars: Enhanced Intracellular Delivery and Efficient NIR Photothermal Therapy Using Ultralow Irradiance. *J. Am. Chem. Soc.* **2012**, *134* (28), 11358–11361. https://doi.org/10.1021/ja304180y.

(66) Zhao, S.; Tian, R.; Shao, B.; Feng, Y.; Yuan, S.; Dong, L.; Zhang, L.; Wang, Z.; You, H. UCNP–Bi2Se3 Upconverting Nanohybrid for Upconversion Luminescence and CT Imaging and Photothermal Therapy. *Chemistry – A European Journal* **2020**, *26* (5), 1127–1135. https://doi.org/10.1002/chem.201904586.

(67) Chen, L.; Mccrate, J. M.; Lee, J. C.-M.; Li, H. The Role of Surface Charge on the Uptake and Biocompatibility of Hydroxyapatite Nanoparticles with Osteoblast Cells. *Nanotechnology* **2011**, *22* (10), 105708. https://doi.org/10.1088/0957-4484/22/10/105708.

(68) Harush-Frenkel, O.; Debotton, N.; Benita, S.; Altschuler, Y. Targeting of Nanoparticles to the Clathrin-Mediated Endocytic Pathway. *Biochemical and Biophysical Research Communications* **2007**, *353* (1), 26–32. https://doi.org/10.1016/j.bbrc.2006.11.135.

(69) Ju, Y.; Guo, H.; Edman, M.; Hamm-Alvarez, S. F. Application of Advances in Endocytosis and Membrane Trafficking to Drug Delivery. *Advanced Drug Delivery Reviews* **2020**, *157*, 118–141. https://doi.org/10.1016/j.addr.2020.07.026.

(70) Cong, V. T.; Houng, J. L.; Kavallaris, M.; Chen, X.; Tilley, R. D.; Gooding, J. J. How Can We Use the Endocytosis Pathways to Design Nanoparticle Drug-Delivery Vehicles to Target Cancer Cells over Healthy Cells? *Chem. Soc. Rev.* **2022**, *51* (17), 7531–7559. https://doi.org/10.1039/D1CS00707F.

(71) Allen, M.; Millett, P.; Dawes, E.; Rushton, N. Lactate Dehydrogenase Activity as a Rapid and Sensitive Test for the Quantification of Cell Numbers *in Vitro*. *Clinical Materials* **1994**, *16* (4), 189–194. https://doi.org/10.1016/0267-6605(94)90116-3.

(72) Blanco, E.; Shen, H.; Ferrari, M. Principles of Nanoparticle Design for Overcoming Biological Barriers to Drug Delivery. *Nat Biotechnol* **2015**, *33* (9), 941–951. https://doi.org/10.1038/nbt.3330.

(73) Shi, D.; Beasock, D.; Fessler, A.; Szebeni, J.; Ljubimova, J. Y.; Afonin, K. A.; Dobrovolskaia, M. A. To PEGylate or Not to PEGylate: Immunological Properties of Nanomedicine's Most Popular Component, Polyethylene Glycol and Its Alternatives. *Advanced Drug Delivery Reviews* **2022**, *180*, 114079. https://doi.org/10.1016/j.addr.2021.114079.

(74) Yang, Y.; Zhu, W.; Dong, Z.; Chao, Y.; Xu, L.; Chen, M.; Liu, Z. 1D Coordination Polymer Nanofibers for Low-Temperature Photothermal Therapy. *Advanced Materials* **2017**, *29* (40), 1703588. https://doi.org/10.1002/adma.201703588.

(75) Wang, S.; Zhang, L.; Zhao, J.; He, M.; Huang, Y.; Zhao, S. A Tumor Microenvironment–Induced Absorption Red-Shifted Polymer Nanoparticle for Simultaneously Activated Photoacoustic Imaging and Photothermal Therapy. *Science Advances* **2021**, *7* (12), eabe3588. https://doi.org/10.1126/sciadv.abe3588.

(76) Du, Y.; Shan, C.; You, Y.; Chen, M.; Zhu, L.; Shu, G.; Han, G.; Wu, L.; Ji, J.; Yu, H.; Du, Y. NIR-II Fluorescence Imaging-Guided Hepatocellular Carcinoma Treatment via IR-1061-Acridine and Lenvatinib Co-Loaded Thermal-Sensitive Micelles and Anti-PD-1 Combinational Therapy. *Chemical Engineering Journal* **2023**, *454*, 140437. https://doi.org/10.1016/j.cej.2022.140437.

(77) Zhou, Y.; Tong, F.; Gu, W.; He, S.; Yang, X.; Li, J.; Gao, Y.-D.; Gao, H. Co-Delivery of Photosensitizer and Diclofenac through Sequentially Responsive Bilirubin Nanocarriers for Combating Hypoxic Tumors. *Acta Pharmaceutica Sinica B* **2022**, *12* (3), 1416–1431. https://doi.org/10.1016/j.apsb.2021.12.001.

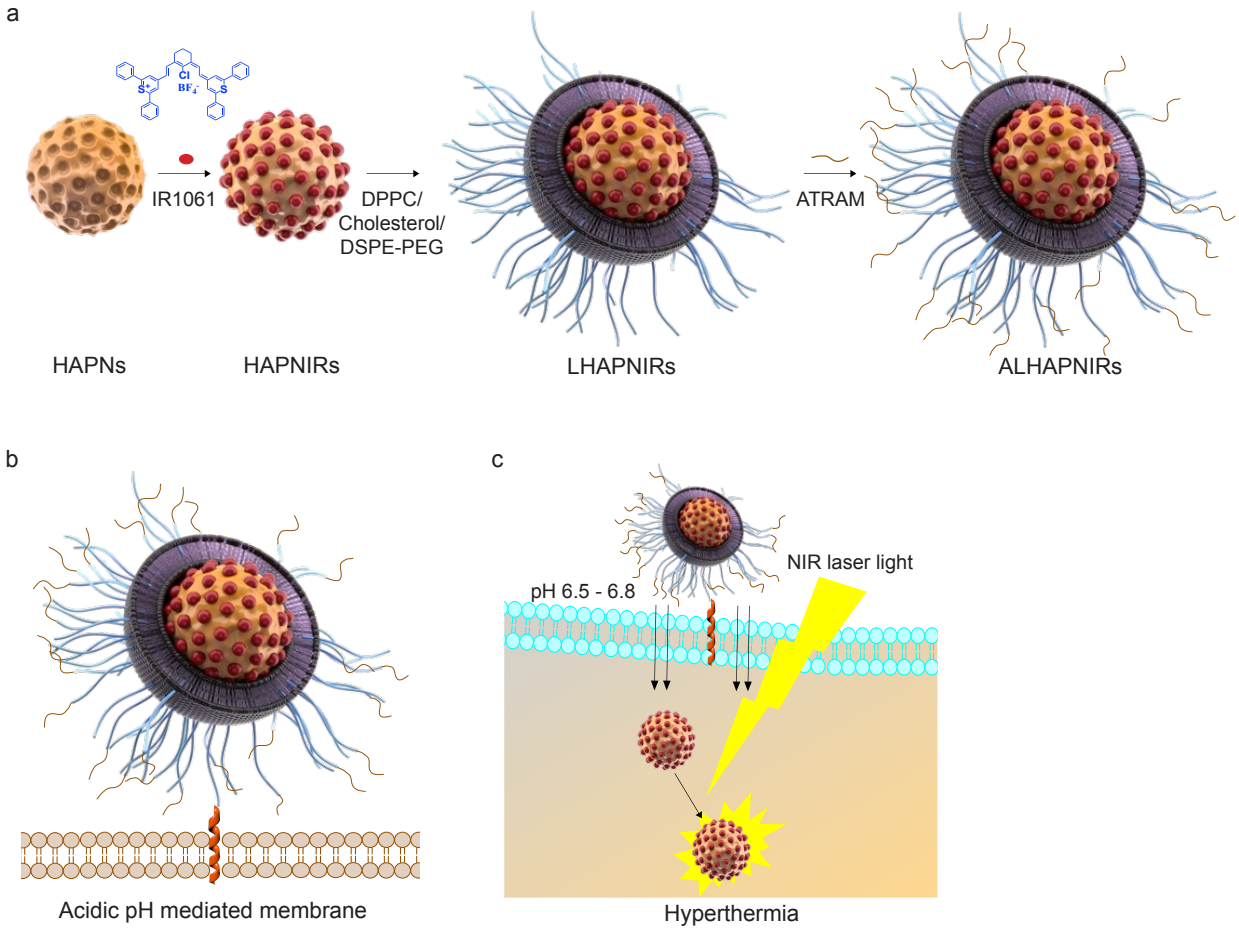

Figure 1. Schematic representation of preparation and mode of action of tumor-targeted hydroxyapaptite nanoparticles. (**a**) The nanoparticles consist of a hydroxyapatite that encapsulates a IR1061 in its pores. The IR1061 loaded hydroxyapatite nanoparticles (HAPNIRs) are then 'wrapped' with lipid/polyethylene glycol (DPPC/cholesterol/DSPE-PEG_{2000}-maleimide). Finally, the IR1061-loaded lipid/PEG coated HAPNs (LHAPNIRs) are functionalized with the acidity-triggered rational membrane (ATRAM) peptide (ALHAPNIRs). (**b**) In the mildly acidic conditions of tumor microenvironment (pH ~6.5–6.8), ATRAM promotes the targeting of ALHAPNIRs to cancer cells. (**c**) ALHAPNIRs are effectively internalized into the cancer cells, where subsequent NIR (980 nm) laser irradiation of the nanoparticles results in substantial cytotoxicity due to the photothermal heat generation.

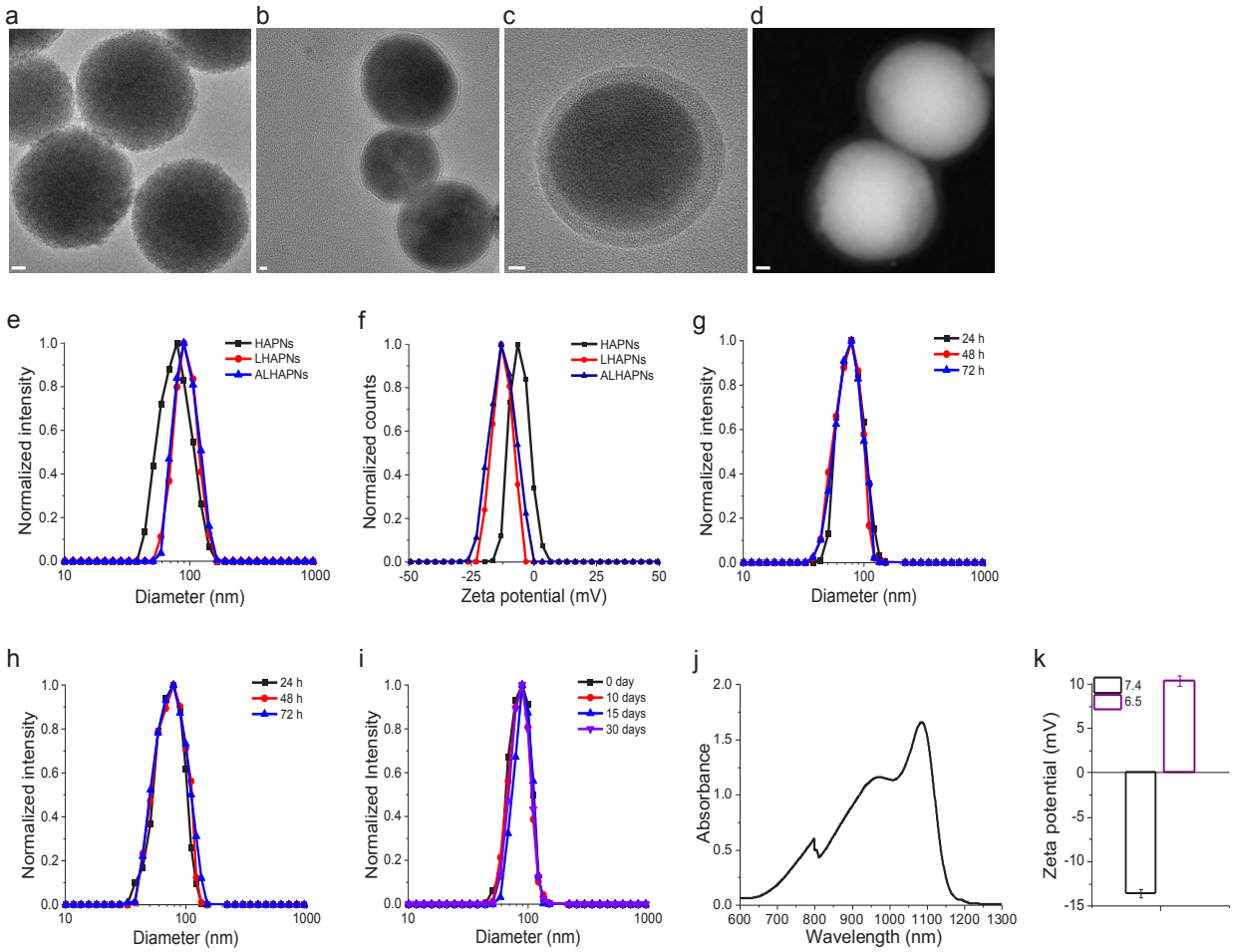

Figure 2. Characterization of hydroxyapatite nanoparticles. (**a-c**) Transmission electron microscopy (TEM) images of the hydroxyapatite nanoparticles (HAPNs) (**a**), lipid/PEG-coated HAPNs (LHAPNs) (**b**) and magnified image of LHAPNs (**c**). (**d**) High-angle annular dark-field scanning transmission electron microscopy (HAAD-STEM) image of LHAPNs. Scale bar = 10 nm. (**e, f**) Size distribution analysis (**e**) and zeta potential measurements (**f**) for HAPNs, LHAPNs and ALHAPNs in 10 mm phosphate buffer (pH 7.4). (**g, h**) Size distribution analysis of LHAPNs in 10 mM sodium acetate buffer (**g**) and complete cell culture medium (**h**). (**i**) Colloidal stability analysis of LHAPNs in 10 mm phosphate buffer over 30 days at 37 °C. (**j**) UV-Vis absorption spectrum of IR1061. (**k**) Comparison of zeta potentials of ALHAPNs at pHs 7.4 and 6.5.

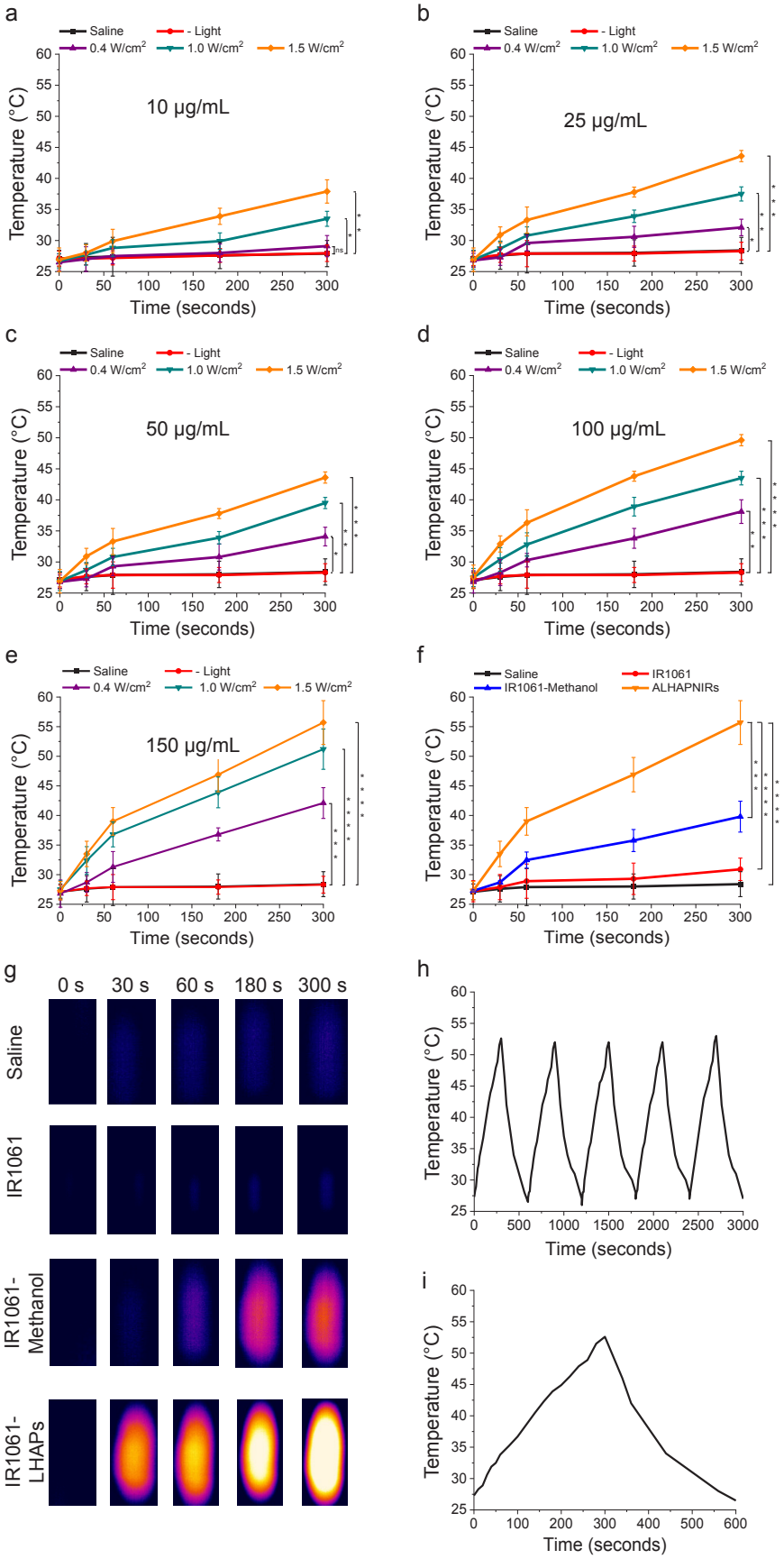

Figure 3. Photothermal properties of IR1061-loaded LHAPNs. (**a-e**) Temperature increases following NIR laser irradiation (0.4-1.5 W/cm^2, 5 min) of LHAPNIRs at nanoparticle concentrations of 10 µg/mL (**a**), 25 µg/mL (**b**), 50 µg/mL (**c**), 100 µg/mL (**d**) and 150 µg/mL (**e**), in 10 mM phosphate buffer (pH 7.4). (**f**) Comparison of NIR laser light (1.5 W/cm^2, 5 min) induced temperature increases in saline, IR1061 and LHAPNIRs samples (22.5 µg/mL IR1061) in 10 mM phosphate buffer (pH 7.4) and IR1061-methanol (22.5 µg/mL IR1061). (**g**) Thermal images of saline, IR1061 and LHAPNIRs samples samples illuminated with NIR laser light (1.5 W/cm^2) for 5 min. (**h**) Photothermal stability of LHAPNIRs (150 µg/mL) monitored over five consecutive NIR laser irradiation (1.5 W/cm^2, 10 min) on/off cycles. (**i**) Photothermal response profile of LHANIRs (150 µg/mL) subjected to NIR laser irradiation (1.5 W/cm^2, 10 min) followed by nature cooling. *$P < 0.05$, ***$P < 0.001$, ****$P < 0.0001$ or non-significant (ns, $P > 0.05$) for comparisons with controls or amongst the different samples.

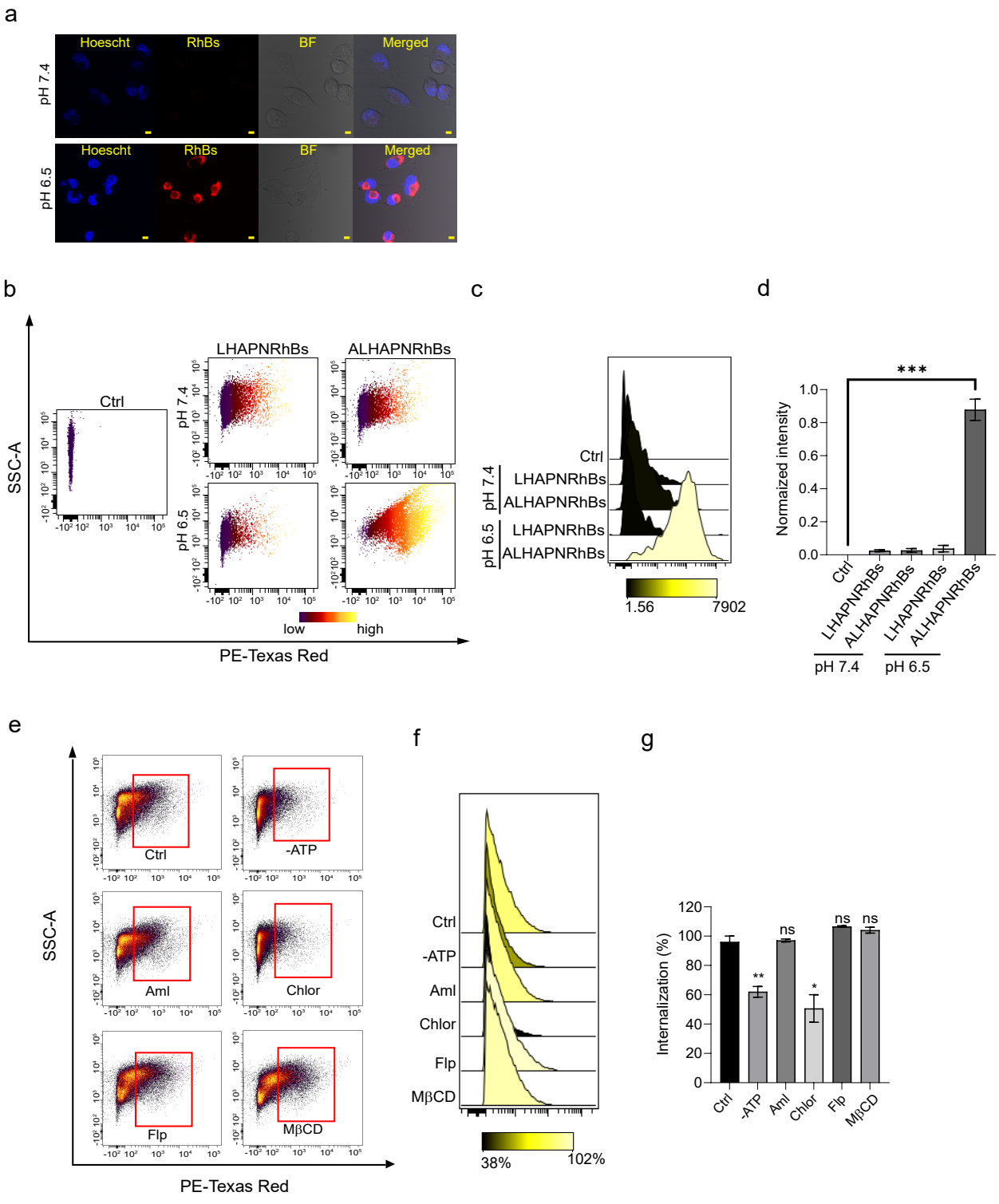

Figure 4. pH-dependent cellular uptake of ALHAPNRhBs. (**a**) Confocal fluorescence microscopy images of MIA PaCa-2 cells incubated with ALHAPNRhBs (0.5 µg/mL) for 4 h at physiological (top panel) or acidic (lower panels) pH. RhB is red-coloured for clarity. Imaging experiments were performed in triplicate and representative images are shown. Scale bar = 10 µm. (**b-d**) Flow cytometry analysis of MIA PaCa-2 cells incubated with and without ATRAM

(LHAPNRhBs or ALHAPNRhBs) at different pH conditions (pH 7.4 and 6.5) which shows uptake of cells in a more acidic environment in 4 h (**c**) Flow cytometry plot shown in the form of histogram for the higher uptake of ALHAPNRhBs at pH 6.5 within 4 h incubation. (**d**) Normalized intensity of the flow cytometry analysis shows more uptake at pH 6.5 within 4 h. (**e**) Flow cytometry analysis of cellular uptake of ALHAPNRhBs in MIA PaCa-2 under conditions of different inhibitors of uptake pathways at pH 6.5. The cells were pretreated with 10 mM sodium azide and 6 mM 2-deoxy-d-glucose (-ATP) or with endocytosis inhibitors-10 μM Chlorpromazine, 5mM methyl-β-cyclodextrin, 5 μM filipin and Amiloride for 15 min at 37 ºC–compared with inhibited uptake in control cells (n = 3). Data were acquired using the FACS ARIA III and analysed using the Cytobank software. (**f**) and (**g**) Histogram and bar graph analysis showing inhibition of -ATP 60% and Chlor 50% amongst other inhibitors. $*P < 0.05$, $**P < 0.001$, $***P < 0.002$ for comparisons with controls or among the different samples.

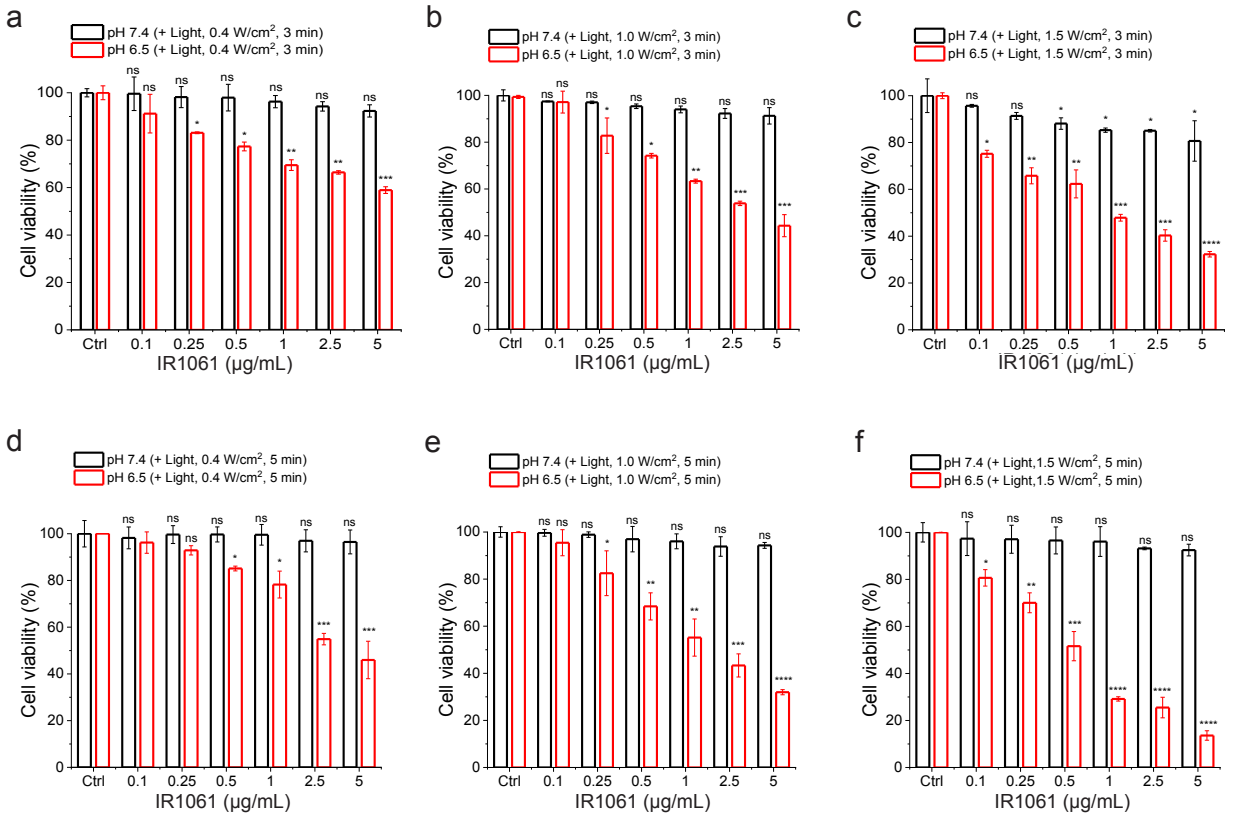

Figure 5. NIR-light triggered cytotoxicity of ALHAPNIRs. (**a-f**) Cell viability of MIA PaCa-2 cells treated with ALHAPNIRs (0.1–5 μg/mL IR1061) for 48 h with subsequent exposure to NIR laser light of different irradiation power densities (0.4–1.5 W/cm^2) at pH 7.4 or 6.5 for durations of 3.0 or 5.0 min. Cell viability in (**a-f**) was measured using the MTS assay, with the % viability determined form the ratio of the absorbance of the treated cells to the control cells (n = 3). *P < 0.05, **P < 0.01, ***P < 0.001, ****P < 0.0001 or non-significant (ns, P > 0.05) compared with controls.

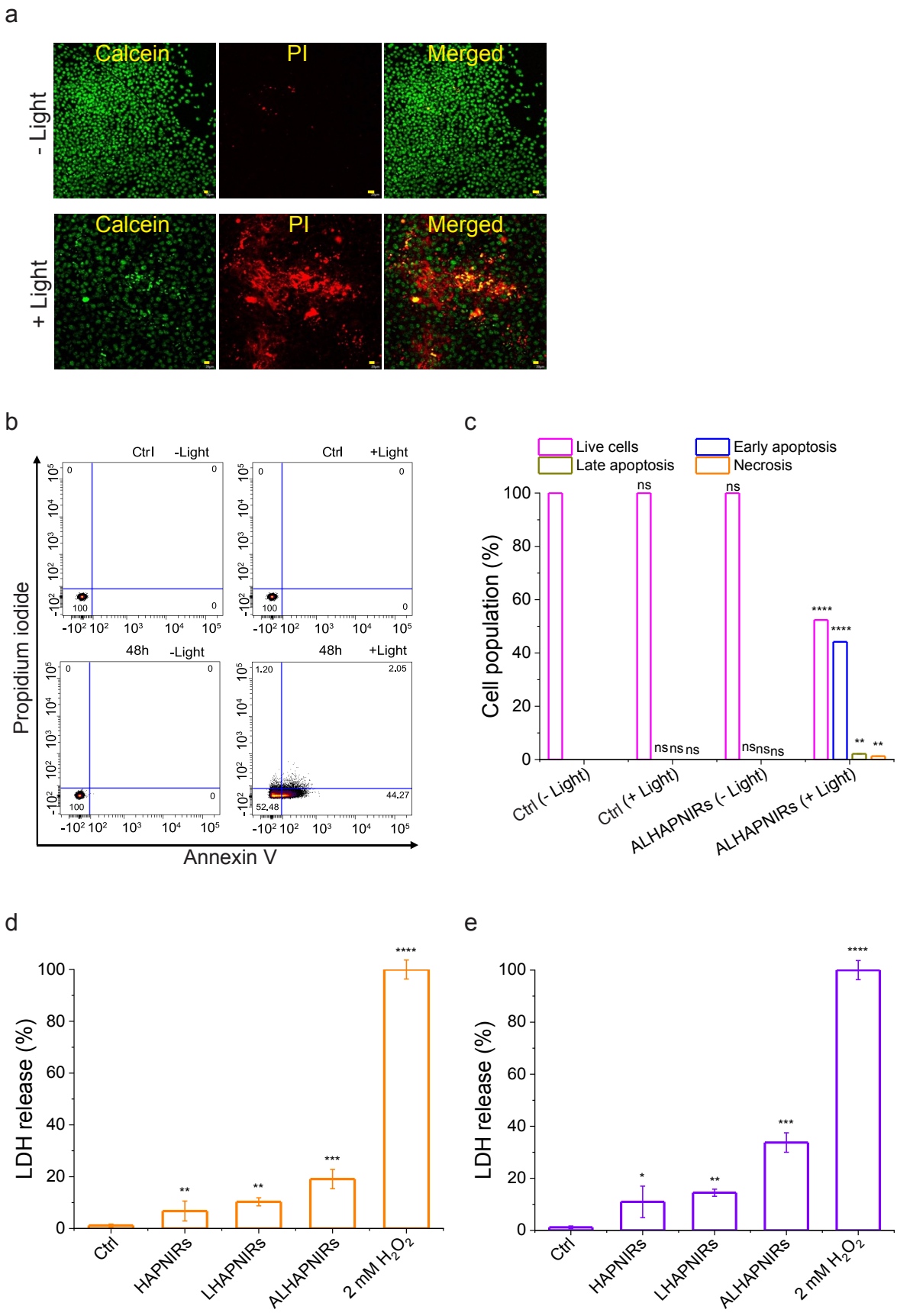

Figure 6. NIR-light triggered apoptosis of ALHAPNIRs. (**a**) Confocal fluorescence microscopy imaging of calcein AM/PI staining with MIA PaCa-2 cells incubated with ALHAPNIRs at 0.5 µg/mL IR1061 for 12 h at pH 6.5 in the absence (- Light) or presence (+ Light) of NIR laser irradiation (1.0 W/cm^2, 3 min). Scale bar = 20 µm. The experiments were performed in triplicate and representative images are shown. (**b, c**) Flow cytometry analysis of annexin V/PI stained MIA PaCa-2 cells that were either untreated (control, Ctrl), or treated with ALHAPNIRs (0.5 µg/mL IR1061) for 48 h at pH 6.5, with exposed to NIR light (1.5 W/cm^2, 5 min). The four quadrants are defined as follows: annexin V^-/PI^- (bottom left), live cells; annexin V^+/PI^- (bottom right), early apoptotic cells; annexin V^+/PI^+ (top right), late apoptotic cells; and annexin V^-/PI^+ (top left), necrotic cells. (**c**) A summary of the incidence of early/late apoptosis and necrosis in the MIA PaCa-2 cells treated with ALHAPNIRs determined from the flow cytometry analysis of annexin V/PI staining in (**b**) (n = 3). (**d, e**) LDH leakage analysis to determine the NIR light induced cell death. ALHAPNIRs were incubated with MIA PaCa-2 cells for a period of 48 h and irradiated for 3- and 5-min. 2 mM H_2O_2 were incubated as a positive control. $^*P < 0.05$, $^{**}P < 0.01$, $^{***}P < 0.001$, $^{****}P < 0.0001$ or non-significant (ns, $P > 0.05$) compared with controls.

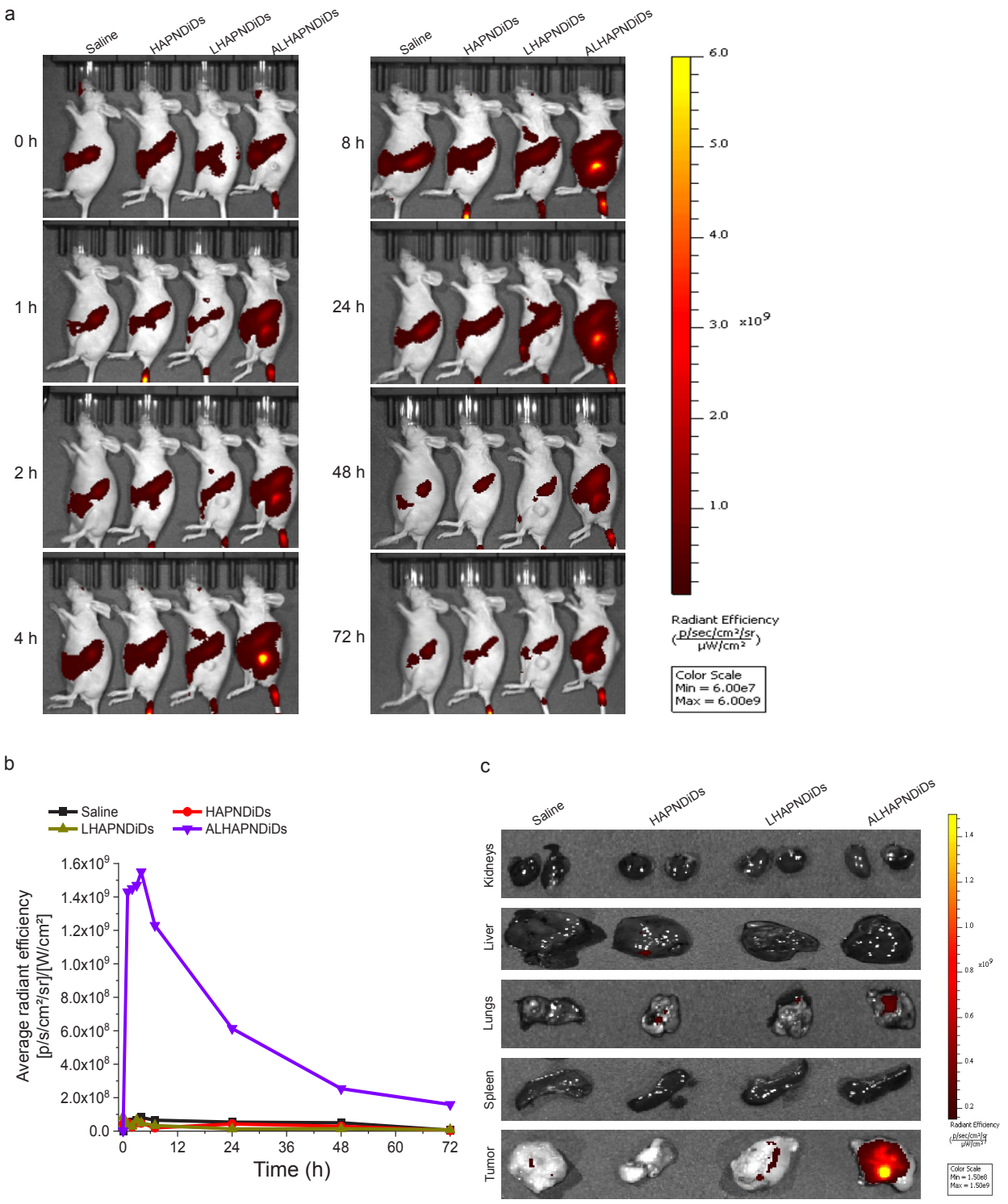

Figure 7. ***In vivo*** **biodistribution and tumor localization of ALHAPNDiDs.** (**a**) *In vivo* biodistribution analysis of HAPNDiDs, LHAPNDiDs and ALHAPNDiDs (2.2 mg/Kg, 0.3 mg/Kg DiD[77]) in MIA PaCa-2 tumor implanted mice after intravenous injection. The images were captured at different time points (0, 1, 2, 4, 8, 24, 48 and 72 h, emission at 720 nm). (**b**) Quantification of fluorescence intensity, measured as an average radiant efficiency using IVIS

Spectrum, in the tumor region. (**c**) *Ex vivo* imaging of isolated tumors and vital organs (kidneys, liver, lungs, and spleen) from mice 72 h after intravenous injection of HAPNDiDs, LHAPNDiDs, and ALHAPNDiDs.

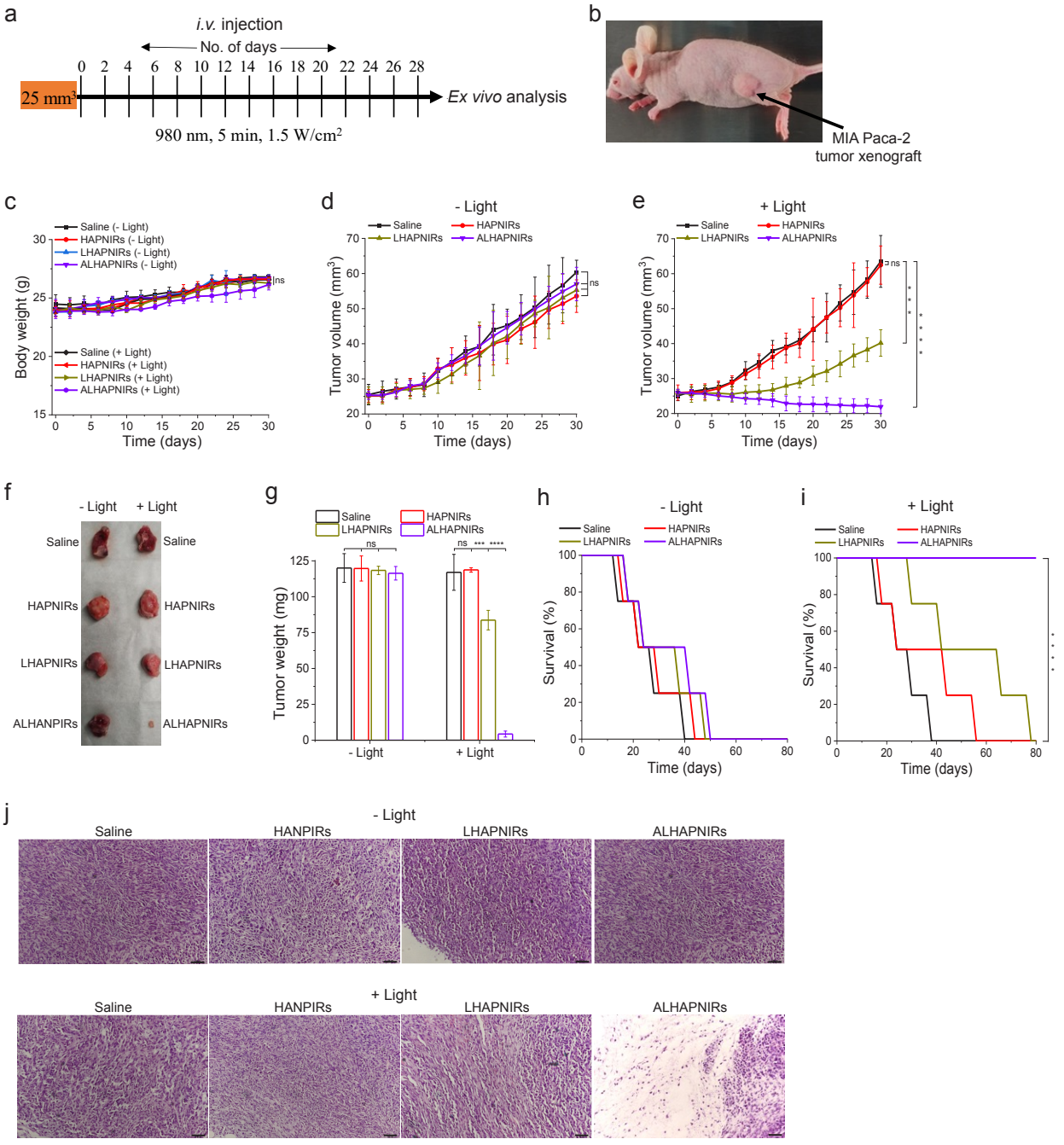

Figure 8. Inhibition of MIA PaCa-2 tumor growth by ALHAPNIRs. (**a**) Design of the tumor reduction studies. Once the tumor volume reached 25 mm^3, the mice were randomized into the different treatment groups (n = 16 per group), which were injected intravenously with saline or HAPNIRs, LHAPNIRs or ALHAPNIRs (22.5 mg/kg nanoparticles, 3.3 mg/kg IR1061). Injections were done every other day for a total of 15 doses, with the first day marked at day 0. Within each treatment group, 8 mice were subjected to NIR laser irradiation (1.5 W/cm^2, 5 min, 980 nm) at 8 h post injection. (**b**) Images of MIA PaCa-2 tumor implanted near the flank of mice. (**c**) Body weight changes of the MIA PaCa-2 tumor-bearing mice in the different treatment groups in the

absence (- Light) or presence (+ Light) of irradiation monitored for the duration of the experiment. (**d, e**) Tumor volume growth curves for the MIA PaCa-2 tumors in the saline and HAPNIRs, LHAPNIRs and ALHAPNIRs treatment groups over 30 days of treatment in the absence (- Light) or presence of the NIR light irradiation (n = 8 per group). (**f, g**) Tumor mass analysis for the saline, HAPNIRs, LHAPNIRs and ALHAPNIRs treatment groups. After 30 days of treatment, four mice per treatment group were sacrificed, and the tumor tissues were isolated and imaged (**f**) and subsequently measured weighed to determine the tumor mass (**g**). (**h, i**) Survival curves for the different treatment groups (saline, HAPNIRs, LHAPNIRs and ALHAPNIRs) over 80 days in the absence (**h**) or presence (**i**) of NIR laser irradiation (n = 4 per group). (**j**) H&E staining of MIA PaCa-2 tumor sections from the different groups (saline, HAPNIRs, LHAPNIRs and ALHAPNIRs) after 30 days of treatment in the absence (- Light) or presence (+ Light) of NIR laser irradiation. *$P < 0.05$, **$P < 0.01$, ***$P < 0.001$, ****$P < 0.0001$ or non-significant (ns, $P > 0.05$) compared with controls.